applied sciences

MDPI

Article

Design and Mechanical Performance of Cylindrical-Coordinate Ti-6Al-4V Octet Lattices: Influence of Outer-Shell Hybridization and Strut Diameter on Compressive Strength

Constantin Romică Stoica [1,2,*], Alexandru Paraschiv [1], Vladimir-Ioan Petrescu [3] and Sebastian Gabriel Bucaciuc [1]

[1] Romanian Research and Development Institute for Gas Turbines COMOTI, 220D Iuliu Maniu Av., 061126 Bucharest, Romania
[2] Faculty of Materials Science and Engineering, National University of Science and Technology Politehnica Bucharest, 313 Independenței Av., 060042 Bucharest, Romania
[3] Fitzpatrick Hall of Engineering, College of Engineering, Aerospace and Mechanical Engineering, Notre Dame University, Notre Dame, IN 46556, USA
* Correspondence: romica.stoica@comoti.ro;

Featured Application

The proposed cylindrical generated lattice structures can support the development of lightweight aerospace turbomachinery components by providing a more uniform mass distribution around the axis of rotation. The findings also provide guidance for the additive manufacturing of complex lattice structures through the selection of suitable geometries, process parameters, and manufacturing strategies.

Abstract

Lattice structures are increasingly used in lightweight engineering applications, particularly in the aerospace, biomedical, and automotive sectors. However, their limited stiffness and narrow linear elastic region can restrict their use in load-bearing applications. This study investigates a hybrid design strategy for improving the compressive performance of Ti-6Al-4V octet lattice structures generated in polar coordinates. Hybrid lattices incorporating a 0.5 mm outer and inner tubular shell and reference lattices without a shell were designed using implicit modeling techniques and manufactured by laser powder bed fusion (LPBF). The mechanical response was characterized through uniaxial compression testing showing an increase in the compressive strength of 900 to 1000% and a strength-to-weight ratio similar to that of bulk titanium in the case of the hybrid samples. Geometrical analysis revealed systematic manufacturing deviations, with all lattice struts exhibiting larger diameters than their nominal dimensions. The hybrid design significantly increased the compressive modulus and yield strength while introducing a moderate increase in mass. Furthermore, the as-printed quality of the polar-generated lattices followed trends reported for equivalent Cartesian-coordinate lattice structures or produced even better results. Overall, the results demonstrate that hybridization can increase compressive strength and modulus significantly while improving the strength-to-weight ratio, with polar lattices exhibiting geometry-dependent trends consistent with Cartesian structures and curved-cell designs providing more uniform volume filling and improved suitability for axisymmetric components.

Keywords: lattice; hybrid; Ti6Al4V; compression; lightweighting; aerospace

Check for updates

Academic Editor: Roberto Zivieri

Received: 20 August 2026
Revised: 20 October 2026
Accepted: 20 October 2026
Published: 22 October 2026

Copyright: © 2026 by the authors. Licensee MDPI, Basel, Switzerland. This article is an open access article distributed under the terms and conditions of the Creative Commons Attribution (CC BY) license.

1. Introduction

Additive manufacturing (AM) has matured into a robust production route for high-performance engineering components, enabling the fabrication of complex geometries that are difficult or impossible to achieve using conventional subtractive or formative processes. This capability has made AM increasingly attractive in aerospace [1–3], biomedical [4], and defense [3,5,6] applications, where lightweight design, part consolidation, and high mechanical performance are critical. In particular, alloys such as Ti-6Al-4V are widely used due to their excellent strength-to-weight ratio and suitability for powder bed fusion processes [7–10].

Reducing fuel consumption and associated emissions requires structural materials and designs that maintain high mechanical performance at reduced mass. In this context, lattice architectures represent an effective strategy for lightweighting. Compared with fully dense materials, metallic lattices can achieve superior specific stiffness, strength, and energy absorption capacity [11,12]. They are commonly used as core structures in sandwich panels, where they provide resistance to compressive and shear loading. When properly designed to mitigate instability phenomena such as buckling, lattice cores can outperform conventional honeycomb structures in both stiffness and compressive strength [3,13–15]. Furthermore, graded lattice architectures [16,17], in which relative density varies spatially according to local load requirements, offer additional opportunities for mass optimization. Beyond structural applications, lattices are also effective energy absorbers under impact and shock loading conditions [5,11,12].

Lattice structures can be manufactured using a range of conventional processes, including machining, casting, laser cutting, and forming techniques [18,19]. However, recent advances in AM technologies have significantly expanded design freedom and manufacturing capability. Processes such as laser powder bed fusion (LPBF), Electron Beam Melting (EBM), Binder Jetting (BJ), Stereolithography (SLA), and Fused Deposition Modeling (FDM) have enabled the production of highly complex cellular architectures with improved geometrical control [10,20–22]. Despite these advances, a comprehensive understanding of the relationship between architecture, process-induced defects, microstructure, and mechanical performance remains essential for reliable structural application.

Cellular materials are commonly classified into foams, honeycombs, and lattices, following the foundational work of Gibson and Ashby [23]. Foams typically exhibit stochastic pore distributions, while honeycombs consist of periodic prismatic cells. Lattices, by contrast, are ordered periodic or semi-periodic structures constructed from repeating unit cells. These lattices can be further categorized based on unit cell topology, size, and spatial arrangement, as well as their mechanical response, which is commonly divided into bending-dominated and stretch-dominated behaviors. Stretch-dominated lattices, such as the octet truss, generally exhibit higher stiffness and strength at equivalent relative density compared to bending-dominated architectures, which makes them more suitable for load-bearing applications. By contrast, bending-dominated structures are often preferred for energy absorption due to their progressive collapse behavior [4,21,24].

Recent studies have highlighted that mechanical performance is strongly influenced by deformation mechanisms and manufacturing constraints [25]. For example, bending-dominated lattices manufactured by LPBF may exhibit post-yield softening due to combined stretching and shear effects in the struts, which challenges classical assumptions regarding their mechanical stability [22]. Octet-truss lattices are particularly notable due to their highly efficient stretch-dominated load-transfer mechanisms [26,27]. In addition, recent work in generative design has introduced modified lattice topologies aimed at improving manufacturability and mechanical performance by adjusting strut connectivity and nodal configurations [4,10,28,29].

These approaches demonstrate that tailored lattice architectures can significantly enhance load-bearing capacity and energy absorption. Furthermore, reconfigurable and programmable lattice concepts have been proposed [30], enabling transitions between bending- and stretch-dominated responses through controlled topology modification, offering new possibilities for adaptive mechanical behavior.

Given the strong dependence of mechanical performance on geometry, significant research effort has focused on lattice optimization strategies. These include aperiodic infill methods [14], spatially graded density distributions [17], and homogenization-based approaches developed to link microscale architecture with macroscale mechanical response. More recently, data-driven and machine learning-assisted design frameworks have been introduced to further enhance structural efficiency. Despite these advances, most existing studies focus on Cartesian-coordinate lattice generation, and limited attention has been given to alternative coordinate systems for lattice construction.

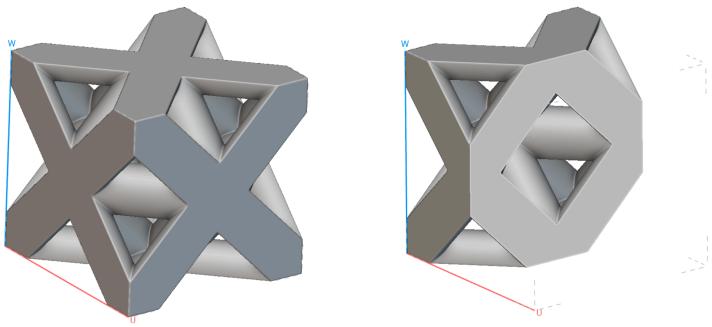
In particular, polar-coordinate-based lattice generation offers potential advantages for components with rotational symmetry and curved geometries, yet its mechanical behavior remains insufficiently explored. Moreover, the combination of polar-generated lattices with hybrid shell reinforcement strategies has not been systematically investigated.

Therefore, the aim of this study is to investigate the compressive behavior of LPBF-manufactured Ti-6Al-4V octet lattices generated in polar coordinates, both with and without a 0.5 mm outer shell. CAD-based implicit modeling is used to design the lattice structures, which are subsequently manufactured using laser powder bed fusion. The geometrical accuracy of the as-built specimens is evaluated using optical stereomicroscopy, while their mechanical response is characterized through uniaxial compression testing. The results show that outer-shell hybridization significantly enhances compressive stiffness, yield strength, and energy absorption, with a moderate increase in mass. In addition, the mechanical response of polar-generated lattices follows trends consistent with those observed in equivalent Cartesian-coordinate lattice systems, which indicates transferable geometric dependencies across coordinate frameworks.

2. Materials and Methods

2.1. Specimen Design and Manufacturing

The specimens were designed using as base cell a Cartesian octet cell type, depicted in Figure 1, that was cylindrically mapped as presented in Figures 2 and 3. Two types of specimens were designed: an open-cell type (Figure 2) and a shelled sample (Figure 3).



(**a**) (**b**)

Figure 1. Octet-cell RVE. (**a**) Isometric view; (**b**) section view.

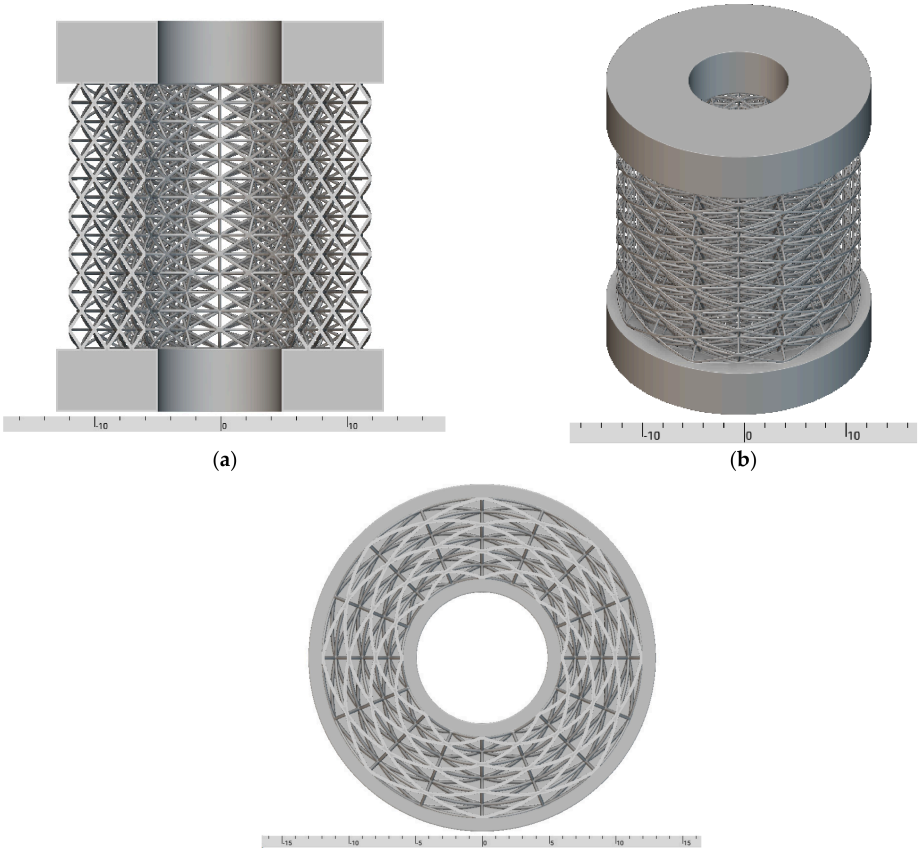


Figure 2. Open-cell sample. (**a**) Vertical plane cross − section; (**b**) isometric view; and (**c**) horizontal plane cross-section.

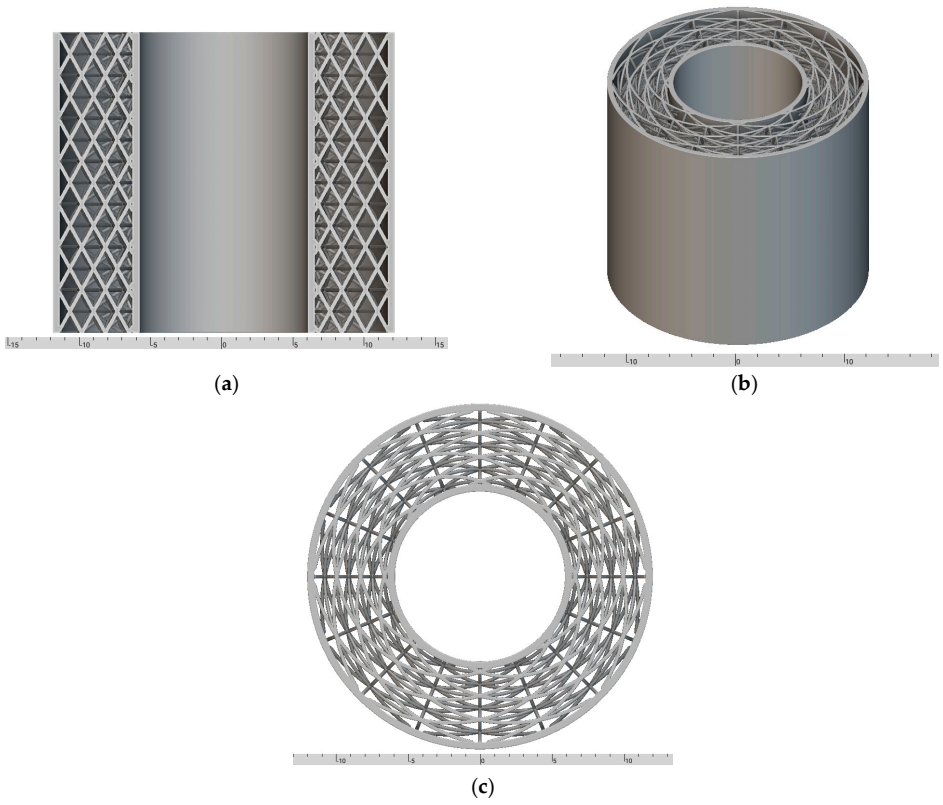


Figure 3. Shelled-cell sample. (**a**) Vertical plane cross-section; (**b**) isometric view; and (**c**) horizontal plane cross-section.

Both samples have a ring shape with an outer diameter of 24 mm for the lattice section, inner diameter of 11.8 mm and total lattice height of 21 mm. The octet-type lattice was generated using nTop software (version 5.47.3, nTopology Inc., New York, NY, USA) and integrated into the specimen using the cylindrical volume lattice method with the curved-cell option. This method creates a cylindrical cell map within a specified volume around the center of mass of that volume. The unit-cell dimensions for both configurations were constant, and they had a radius of 2 mm and a height of 3 mm. The cells were distributed at 8 arc counts from the center of the specimen, and the tolerance was set to 0.001 mm. For both sample configurations, the strut diameter was varied between 0.21 and 0.29 mm to assess its influence on the mechanical properties. The open-cell samples were manufactured with 5 mm thick plates on the top and bottom sides, with an outer diameter of 26 mm and an inner diameter of 9.8 mm for load introduction. The plates were machined on a 3-axis milling machine to achieve plane-parallel surfaces.

The shelled specimens have two walls of 500 µm thickness (interior and exterior) merged with the latticed core via a Boolean operation. No radius was applied at the interface of the lattice with the inner and outer walls. In addition, shell-only configurations featuring exclusively these boundary walls without an internal lattice core were included in the experimental matrix to evaluate the independent contribution of the structural skin. The specimens' design densities are reported in Table 1 and were determined using the nTop software.

Table 1. As-designed sample density.

Sample Type and Code	Relative Density [%]	Density [kg/m^3]
0.21_O	5.64	249.94
0.23_O	6.71	297.47
0.25_O	7.87	348.84
0.27_O	9.11	403.77
0.29_O	10.38	460.04
shell-only	24.4	1082.8
0.21_S	26.00	1151.91
0.23_S	27.13	1202.00
0.25_S	28.42	1259.06
0.27_S	29.81	1320.50
0.29_S	31.24	1384.00

O stands for open cell, and S stands for shelled specimens.

The specimens were manufactured using a DMG Mori's Lasertec 30 SLM machine (upgraded first-generation machine, DMG Mori Romania, Pitesti, Romania) and the Ti-based alloy Ti-6Al-4V ELI (powder manufactured by Heraeus Additive Manufacturing GmbH, Hanau, Germany), with powder size distribution as follows: D10 = 25.6 µm, D50 = 36 µm, and D90 = 47.6 µm. The process parameters used for the specimens' manufacturing process were laser power 279 W, scanning speed 1170 mm/s, 40 µm layer thickness, hatch distance of 0.11 mm, and scanning strategy at 0° with a 90° rotation. The calculated volumetric energy density (VED) was 54.2 J/mm^3. A Ti-6Al-4V building plate was used to manufacture the specimens. The chemical composition of the alloys is presented in Table 2.

Table 2. Feedstock chemical composition.

Element (wt.%)	Al	V	Fe	O	N	H	C	Y	Other, Total	Ti
Specification	6–6.5	3.5–4.5	≤0.25	≤0.1	≤0.03	≤0.12	≤0.08	≤0.005	<0.1	Balance

For the analysis stage, the Gibson-Ashby model presented in [31] was used, where ρ_f and ρ_s are the equivalent densities of the octet lattice metamaterial and of the solid, respectively; E_f and E_s are the Young Moduli of the foam (octet lattice) and of the solid, respectively; and σ_f and σ_s are the compressive strengths of the foam and solid, respectively. C_1 and C_2 are the Gibson–Ashby constants, which incorporate the proportionality properties and have values of 0.62 and 0.33, respectively, for the octet cell.

$$\rho_r = \frac{M_{lattice}}{M_{Solid}} \quad (1)$$

$$\rho_r = \frac{\rho_f}{\rho_s} \quad (2)$$

$$\frac{E_f}{E_s} = C_1(\frac{\rho_f}{\rho_s})^2 \quad (3)$$

$$\frac{\sigma_f}{\sigma_s} = C_2(\frac{\rho_f}{\rho_s})^{1.5} \quad (4)$$

The Gibson-Ashby model serves as a reference for scaling relationships rather than providing exact predictions of the mechanical behavior of the investigated cylindrical architectures. Although the octet topology is classically considered stretch-dominated, the curved-beam geometry investigated in this study may introduce additional bending and rotational deformation of the struts. Consequently, the mechanical response can exhibit a mixed stretch–bending character, particularly at lower relative densities and smaller strut diameters. Therefore, the Gibson-Ashby scaling exponents used in this study should be interpreted as empirical relationships describing the investigated structures.

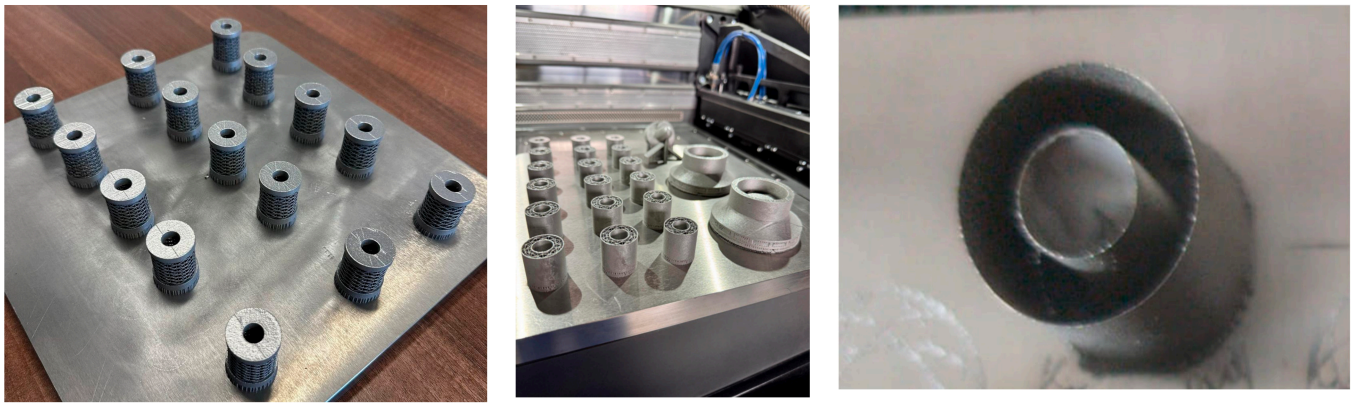
Another metric used to assess the structural efficiency of the octet lattice was $\frac{\sigma_{MAX}}{\rho}$, which represents the ratio between the maximum compressive stress and the relative density of the lattice sample. The results were compared with the fully dense material properties obtained from [32].

For both specimen batches, the building plate was preheated to 180 °C, and argon 4.8 was used as the shielding gas. All specimens were built with a vertical build orientation; the central axis of the samples was aligned with the Z-axis of the LPBF machine (Figure 4). The samples were fixed on the printing machine plate using 3 mm support material to allow mechanical separation. At the end of the manufacturing stage, two batches of specimens were obtained, each containing 15 specimens (3 specimens for each strut diameter and design type). After manufacturing, all specimens were mechanically removed from the building plate, and the support material was removed by grinding. The bottom faces of the shelled specimens were ground slightly to provide plane-parallel faces. The open-cell batch was machined on both top and bottom surfaces to obtain parallelism between the support and loaded face. The specimens were tested in as-built state, without any heat treatment applied.

2.2. Mechanical Testing

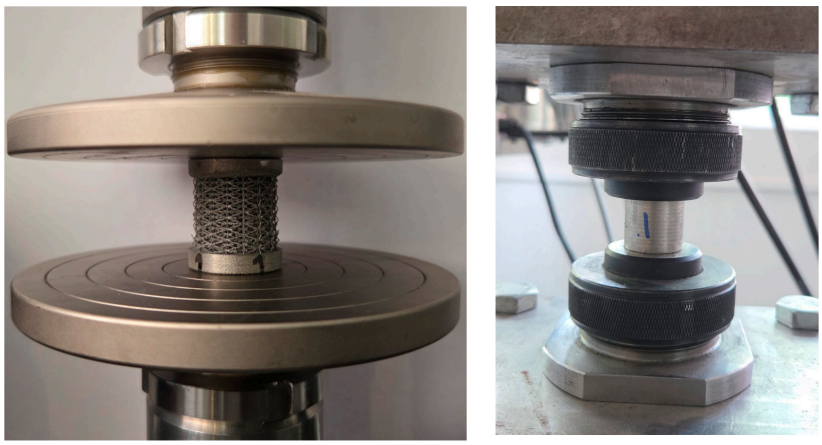
Compression testing was conducted according to ISO 13314:2011 [33] and ASTM E9 [34] using an Instron 3369 (Instron, Norwood, MA, USA) universal mechanical testing machine equipped with a 50 kN load cell and compression plates for the open-cell samples and an Instron 8802 (Instron, Norwood, MA, USA) hydraulic universal testing machine equipped with a 250 kN load cell for the shelled specimens (Figure 5). All tests were performed at room temperature (23 °C ± 2 °C), with a testing speed of 3 mm/min corresponding to a 0.14 mm/mm/min strain rate until a 7 mm elongation was achieved for each specimen. The samples were loaded in the build direction. Open-cell samples were machined on the top and bottom sides to ensure surface parallelism using a 3-axis milling

machine, and for the shelled samples, grinding on a rotary plate machine was involved. The compressive modulus was determined using measurements made from a preload of 50 N for the open-cell samples and 500 N for the shelled specimens. The preload value for the shelled specimens was selected at a value of 500 N to eliminate initial gaps and minimize specimen movement or misalignment at the beginning of the test, particularly given the open-cell architecture and the presence of the shell. The preload represents only 0.7–1% of the peak loads experienced during testing; therefore, the preload was used primarily to eliminate initial gaps and ensure reproducible contact without loading the samples to a significant level. The selection of the testing machines was made based on the load-cell capacity and stiffness of the testing machine, based on the expected peak forces of the two samples' configurations, to ensure a safe operation and accuracy of measurements.



(**a**) (**b**) (**c**)

Figure 4. Pictures of the manufactured samples. (**a**) Open cell; (**b**) shelled specimens; and (**c**) shell-only.



(**a**) (**b**)

Figure 5. Samples with (**a**) open cell on Instron 3369 and (**b**) outer shell on Instron 8802 between the compression plates.

2.3. Microscopy

Visual inspection using the Motic SMZ-171 stereomicroscope with digital camera DFK NME33UX264 (The Imaging Source Gmbh, Bremen, Germany.) and dedicated analysis software NIS-Elements (Nikon Instruments Inc., Melville, NY, USA), version 5.0, was conducted on the specimen's strut diameter, wall thickness and cell parameters before mechanical testing on as-printed specimens, without any preparation. The measurements were used to determine the actual strut diameter and lattice parameters to assess the attainable tolerances with the LPBF process.

Metallographic inspection was performed on etched samples with Kroll's reagent and assessed using light optical microscopy images taken at 200× magnification using a Zeiss Axio Vert.A1 MAT microscope (Carl Zeiss AG, Oberkochen, Germany).

Scanning electron microscopy (SEM) was used to evaluate the surface morphology, dimensional accuracy, and structural integrity of the additively manufactured Ti-6Al-4V lattice specimens. Observations were performed using a Quanta 250 (FEI Company, Hillsboro, OR, USA) scanning electron microscope at an accelerating voltage of 15 kV, a working distance of approximately 10 mm, and magnifications between 150× and 400×. Both as-built and compression-tested specimens were examined. Particular attention was paid to manufacturing-related surface features and defects, including balling, adhered or partially melted powder particles, surface irregularities, cracks, and porosity. SEM images were also used to measure the strut diameters and assess dimensional deviations within the lattice structure. In addition, metallographically prepared transverse cross-sections were analyzed to identify internal defects, such as pores, cracks, lack-of-fusion regions, and other process-related discontinuities.

2.4. CT Scan

Computed tomography inspection used the ZEISS METROTOM 1500 (Carl Zeiss AG, Oberkochen, Germany) using a voxel size of 15.43 µm. The analysis was conducted in the Zeiss Inspect 2026. The measurements were used to determine the pores in the struts and outer shell to assess the attainable quality with the LPBF process of such thin structures.

3. Results

3.1. Compression Test Results

3.1.1. Open-Cell Samples

In Figure 6, the stress–strain curves of the open-cell lattices are presented. The influence of strut diameter on the maximum compressive stress and modulus is linear and directly proportional. The increase in strut diameter generates an increase in mechanical properties. The failure of the lattice happens with the collapse of an entire lattice floor, then the load is redistributed and the next floor collapses, and the process continues until densification. The peaks in the stress–strain curves represent the maximum load at which a lattice floor fails and the onset of collapse. This type of failure is common for stretch-dominant cell types such as the octet.

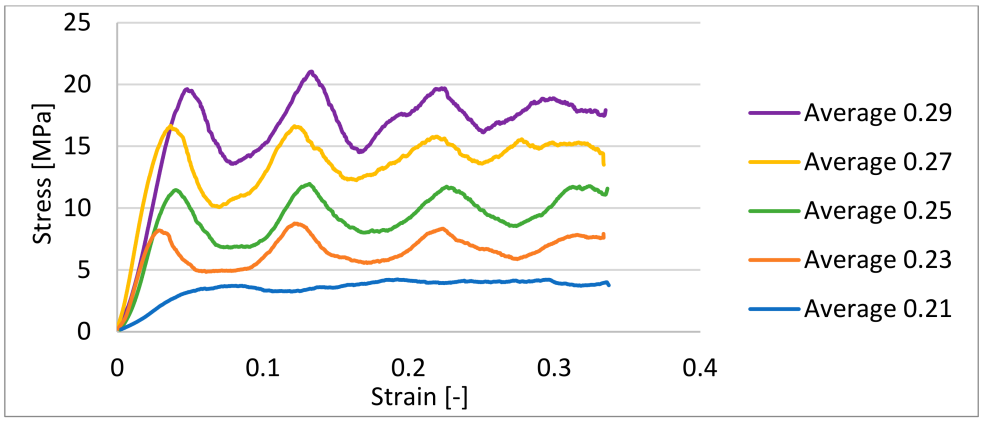


Figure 6. Average stress–strain curves of the open-cell samples.

For comparison with the experimental results, the Gibson–Ashby relationship was evaluated continuously over the investigated relative-density range and is plotted as a solid line in Figure 7. The experimental measurements are shown as discrete markers,

which allows the deviation between the measured response and the theoretical scaling relationship to be directly assessed. The comparison provides an indication of the extent to which the experimentally manufactured lattices follow the idealized density–property scaling relationship, while deviations may be associated with the influence of the actual lattice geometry and manufacturing-induced imperfections. In reality, the dimensional deviation is a source of error; thus, the diameter of the strut must be controlled to obtain precisely tailored mechanical properties. Further chapters investigated the dimensional accuracy of the lattice, and a higher diameter was obtained for the struts, with good accuracy of the cell dimensions. Thus, it is very important to measure the strut diameter by avoiding surface defects that can introduce errors (e.g., adhered powder). However, the cylindrical generated lattice has a similar trend to the Gibson-Ashby model, and measurements can be calibrated based on the actual strut diameter.

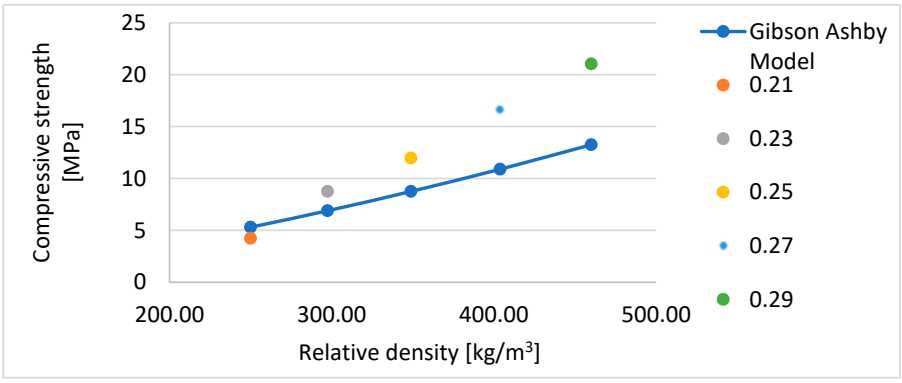


Figure 7. Comparison of the open-cell sample experimental results (point data) and the Gibson–Ashby model prediction (solid line).

A very important metric is the specific compressive strength, shown in Figure 8, where a comparison of the open-cell samples and bulk AMed titanium is presented. The specific compressive strength of the lattice is set at around 10 to 20% of the titanium reference for the range of strut diameters investigated. Considering that the strut diameter is higher than nominal in all configurations, these values are even lower for the open-cell samples. In Figure 9, the compressive modulus obtained for each open-cell sample is plotted, and the influence of strut diameter is directly proportional, with an increase in strut diameter creating an increase in the compressive modulus. Thus, the lattices represent a convenient way to reduce the mass of the components for engineering applications, but the efficiency is less than that of bulk materials.

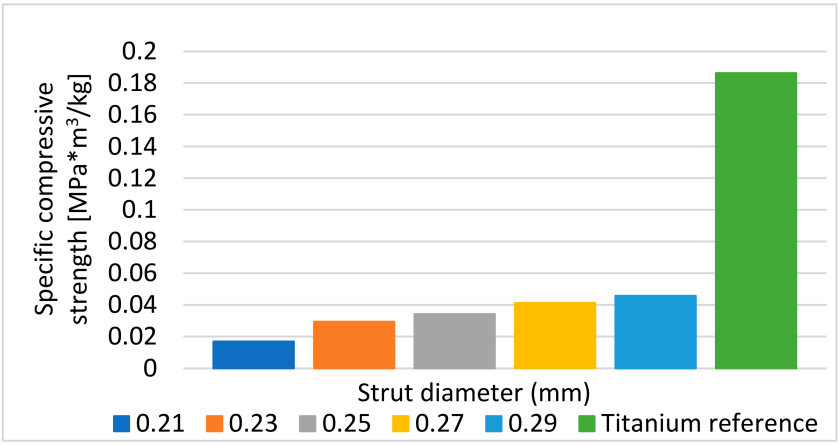


Figure 8. Comparison of the open-cell samples with the bulk titanium specific compressive strength.

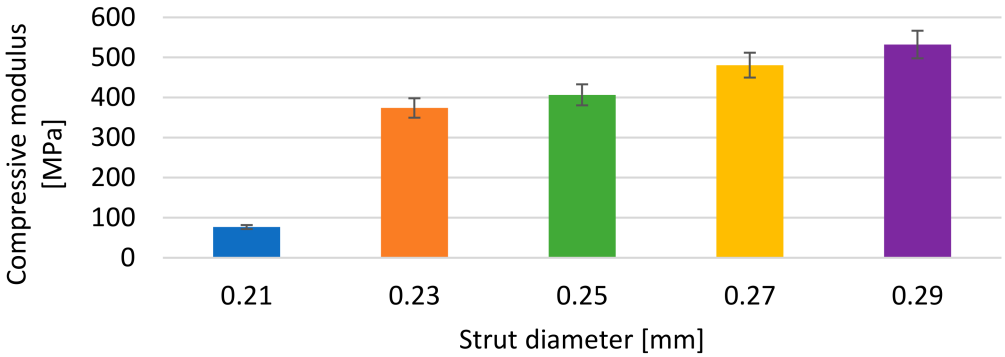


Figure 9. Compressive modulus obtained for open-cell samples.

The specific compressive modulus does not follow the same trend; in Figure 10, the 0.23_O sample shows the highest structural efficiency and the 0.21_O shows the lowest, and 0.25 to 0.29 have almost the same specific strength.

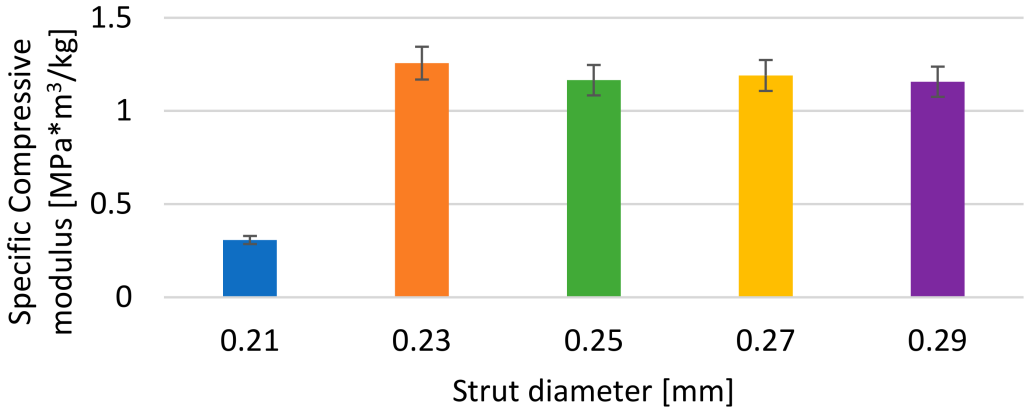


Figure 10. Specific compressive modulus of the open-cell samples.

The O_0.21 sample showed the smallest values because it was the sample with the smallest diameter of the struts, and this dimension is at the edge of manufacturability, which results in samples with numerous locations with fractured members. The specific compressive modulus is at its maximum for the O_0.23 sample, while the maximum compressive strength is obtained by sample O_0.29.

3.1.2. Shelled Samples

The behavior of the shelled samples is changed drastically from the open-cell samples. The presence of the walls is creating a different stress–strain curve (Figure 11). The curves present a much higher peak force and peak stress and a sudden drop after shell crippling, followed by a steady increase in force and stress due to densification.

The shelled samples have a steady collapse behavior after the first peak with densification, opposite to the open-cell samples, where the first peak is repeated and represents the failure load of an entire lattice floor.

A comparison with the Gibson-Ashby model was made, as shown in Figure 12, using the relative densities of the shelled samples to plot the Gibson–Ashby equation as a solid line and the experimentally obtained data with discrete points representing the measured compressive strength. The comparison of the theoretical values obtained for the same densities serves as a reference baseline corresponding to the same relative-density range, allowing the mechanical properties obtained after applying the shelling strategy to be compared with the properties predicted by the classical cellular-solid scaling relationship. This comparison shows that shelled specimens, because of the combined lattice–shell

architecture and its additional load-transfer mechanisms, have superior performance over the same octet open cell over the same relative-density range. The ratio between the experimental values and the model predictions indicates a three-to-four-fold difference in compressive strength for the investigated configurations. However, this difference should be interpreted as a deviation from the reference prediction rather than a directly measured improvement over an octet structure of equivalent relative density, as no such counterpart was experimentally tested in this study.

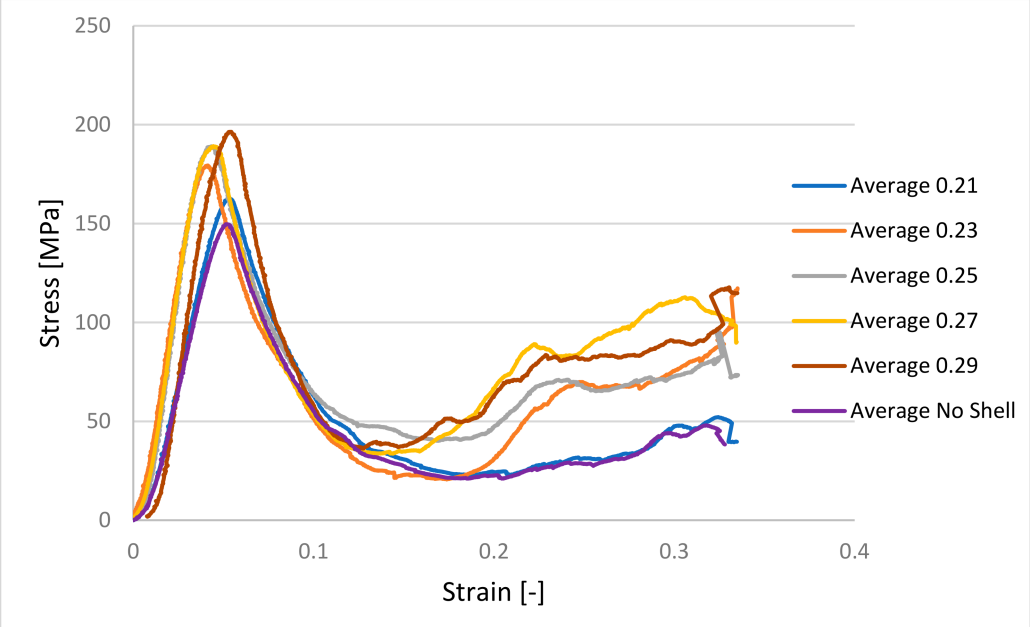


Figure 11. Average stress–strain curves of the shelled samples.

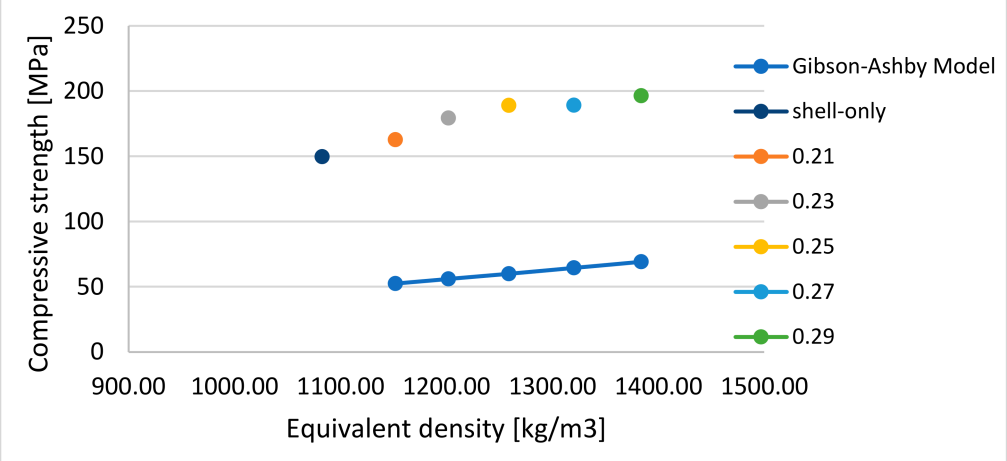


Figure 12. Comparison of the shelled samples' experimental results (point data) and the Gibson-Ashby model prediction (solid line).

The efficiency of the shelling strategy compared to the open-cell samples was measured using the specific compressive strength and compared with that of bulk titanium (Figure 13). This time, the values approach those of bulk titanium and are much higher than those of the open-cell samples. A direct proportionality between the strut diameter and compressive modulus is established for the shelled samples, with sample 0.29_S showing the highest compressive strength of 196 MPa. However, the specific compressive

strength does not follow the same trend, with sample 0.25_S showing the highest specific compressive strength.

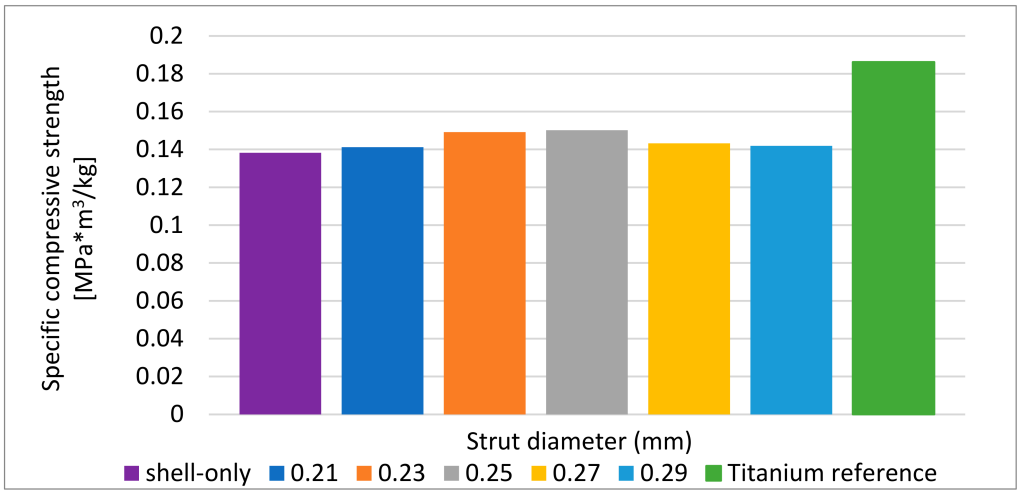


Figure 13. Comparison of the shelled samples with the bulk titanium specific compressive strength.

A similar trend with the specific compressive strength can be observed for the compressive modulus (Figure 14) and specific compressive modulus (Figure 15). It should be noted that the compressive modulus was determined from the initial linear portion of the compressive stress-strain curve and therefore represents the effective structural modulus of the lattice specimens rather than the elastic modulus of bulk Ti-6Al-4V. Sample 0.25_S showed the maximum values of 6.2 GPa and 5.1 MPa*m^3/kg.

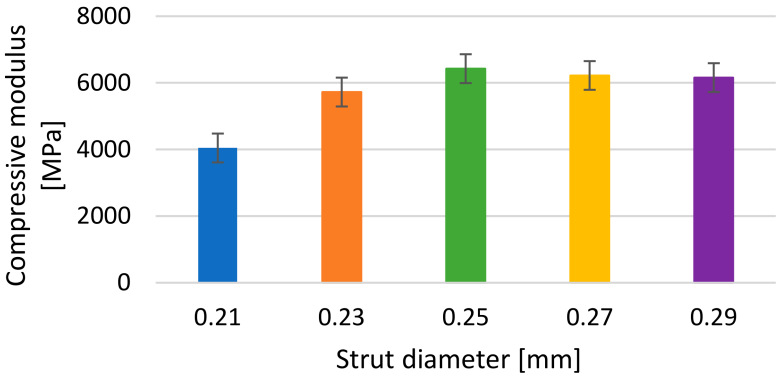


Figure 14. Compressive modulus of shelled samples.

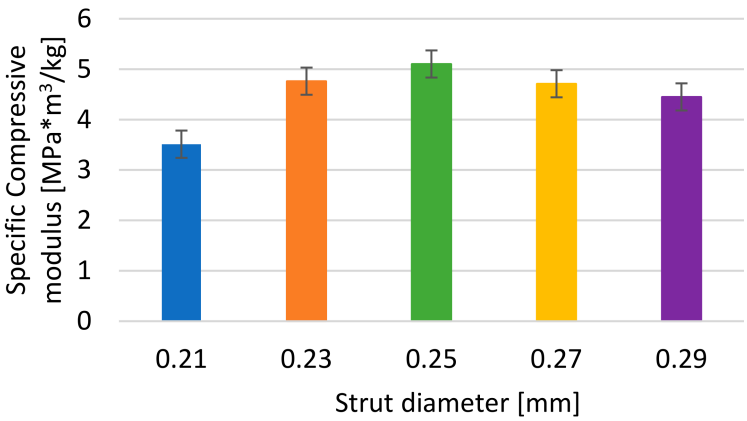


Figure 15. Specific compressive modulus of shelled samples.

3.2. Microscopy and CT Scan Results

SEM micrographs with shell-only measurements of the walls and strut thicknesses for the 0.21, 0.23, 0.25, 0.27, and 0.29 closed-shell samples are presented in Figure 16. The evaluation of these specimens in a shell-only configuration provides insight into the manufacturing accuracy of the LPBF process when fabricating thin, solid features in conjunction with delicate lattice struts.

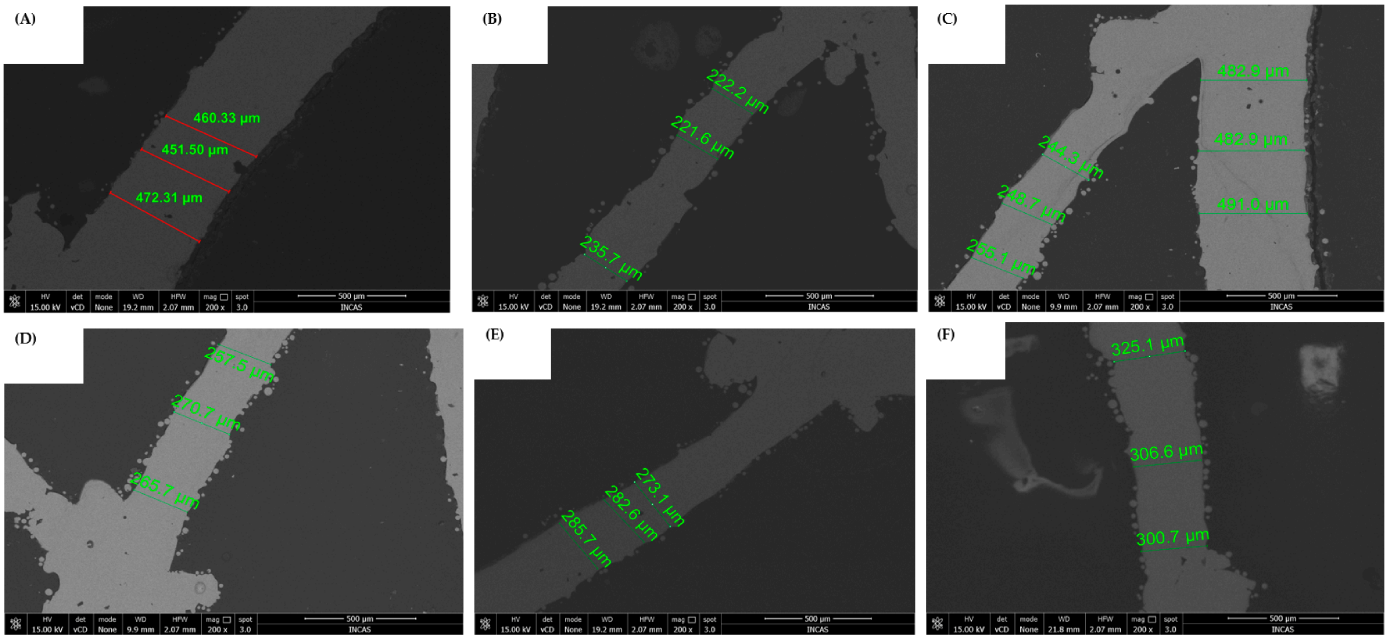


Figure 16. SEM micrographs with (**A**) shell-only measurements of the walls and strut thicknesses of (**B**) 0.21; (**C**) 0.23; (**D**) 0.25; (**E**) 0.27 and (**F**) 0.29 closed-shell samples.

Dimensional characterization revealed systematic deviations from the CAD nominal model across all shelled configurations. The shell-only specimen (Figure 16A) exhibited an average wall thickness of approximately 461.89 µm, reflecting a slightly lower thickness relative to the targeted 500 µm. By contrast, the internal lattice struts generally showed oversizing due to powder particle agglomeration: the 0.21 configuration (Figure 16B) averaged 226.5 µm, while the 0.23 µm (Figure 16C) measured 249.4 µm on the struts alongside a localized wall reading of 485.6 µm, which highlights regional geometric variations. This trend continued across denser architectures, with measured strut averages reaching 264.63 µm for the 0.25 mm target (Figure 16D) and 280.4 µm for the 0.27 mm target (Figure 16E). Finally, the 0.29 configuration (Figure 16F) recorded an average thickness of 310.8 µm.

In Figure 17, an example of the measurement procedure of the open-cell sample is presented for the inclined, radial and cell dimensions. In Figure 17d, a photo showing adhered powder on the lower side of the inclined struts is presented. These adhered powder particles make the dimensional analysis difficult and lead to larger diameters being measured with this method. Commas are used as decimal signs.

Table 3 summarizes the measurements of all the open-cell samples, showing that the absolute differences are lower than 100 µm, an acceptable tolerance for laser powder bed fusion (LPBF) technology.

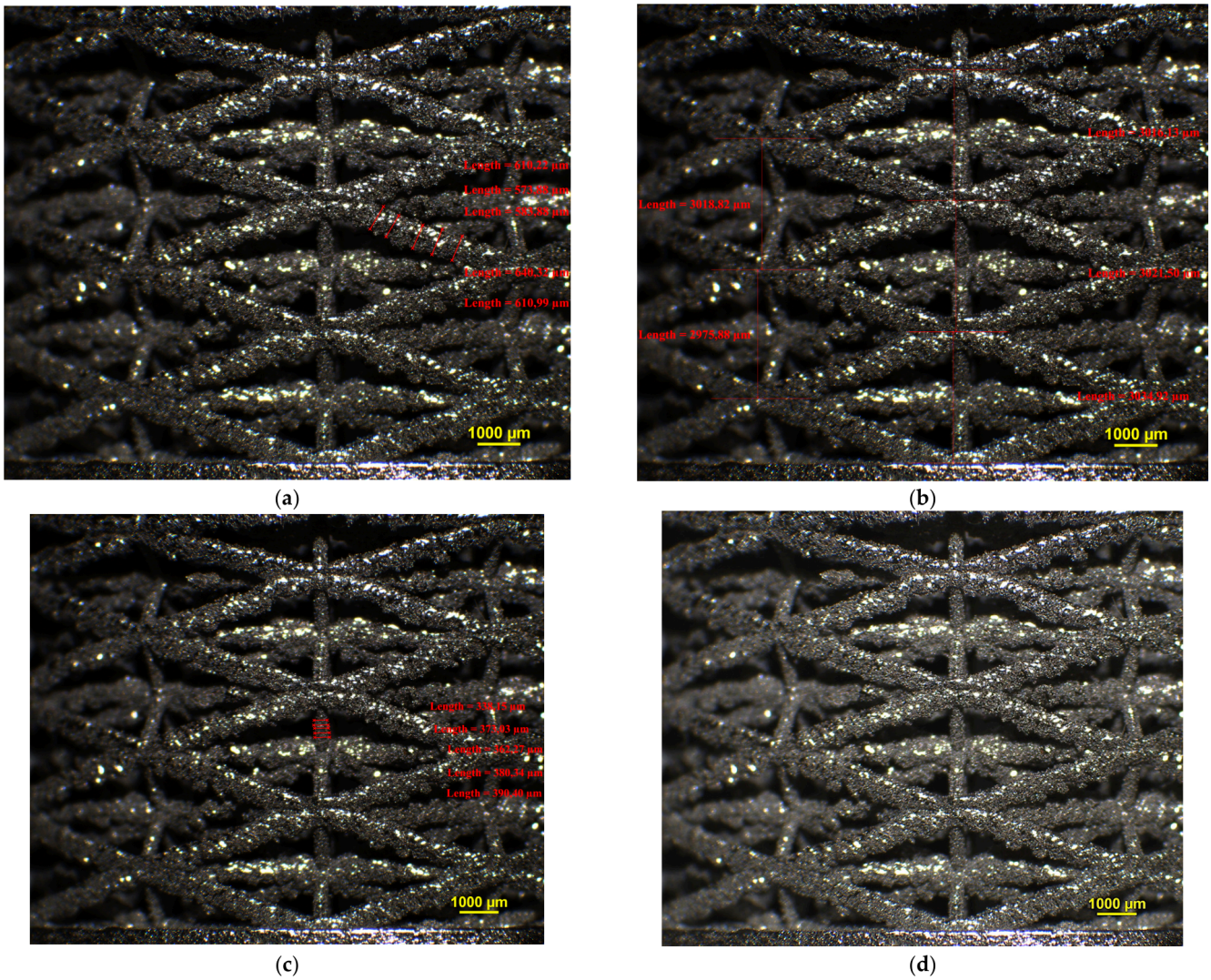


Figure 17. Images of open-cell sample 0.29 with (**a**) inclined struts measurements; (**b**) cell height measurements; (**c**) radial struts measurements; and (**d**) particles adhered on the lower side of the inclined struts.

Table 3. Dimensional analysis of the as-printed open-cell lattice.

Sample Type and Code	Radial Struts Diameter [µm]	Inclined Struts Diameter [µm]	Cell Height [µm]	Radial Struts Diameter Average Deviation [µm]	Cell Height Average Deviation [µm]
0.21_O	282.83	408.69	2954.16	72.83	−45.84
0.23_O	276.49	489.66	3019.33	46.49	19.33
0.25_O	304.14	451.09	3011.66	54.14	11.66
0.27_O	338.13	554.19	3016.66	68.13	16.67
0.29_O	357.82	608.14	3018.33	67.82	18.33

The measured values indicate that all closed-shell specimens exhibited small dimensional deviations from the target strut thickness. The octet lattice presents surface imperfections, including increased roughness caused by powder particle adhesion from the powder bed and the staircase effect and inclination of the struts relative to the printing direction. These defects are common in the laser powder bed fusion (LPBF) manufacturing process.

Although dimensional deviations were identified in all specimens, they remain within the acceptable accuracy range typically reported for metallic parts produced by laser powder bed fusion (LPBF). Furthermore, the deviations measured in this study are smaller than many of the lattice strut diameter deviations reported in [7,35] and [27].

These manufacturing deviations are particularly relevant for the investigated 6–10% relative-density lattices because the small strut dimensions make local deviations proportionally more significant, with a 50 μm deviation representing roughly 17–25% of the strut diameter. Adhered particles can increase the local effective strut thickness and surface roughness, while dimensional deviations can modify the local load-bearing cross-section and consequently affect the stiffness, strength, and failure behavior. Therefore, the measured mechanical response represents the behavior of the as-manufactured structures and may differ from that of an idealized numerical geometry. These effects could be mitigated in future studies by optimizing process parameters, powder characteristics and build orientation together with appropriate post-processing to mitigate these manufacturing imperfections. Optical microscopy of the as-built Ti-6Al-4V processed via LPBF (Figure 18) revealed a highly non-equilibrium microstructure dominated by a fully acicular α′ martensitic phase contained within coarse, columnar prior β grains. Due to the high cooling rates inherent to the LPBF process, the high-temperature β phase undergoes a diffusionless transformation, yielding a dense, hierarchical network of interlocking α′ needles with sub-micron lath thicknesses. Typically, LPBF parts require post-process heat treatment to optimize ductility, but the post-processing of lattices falls outside the scope of this study.

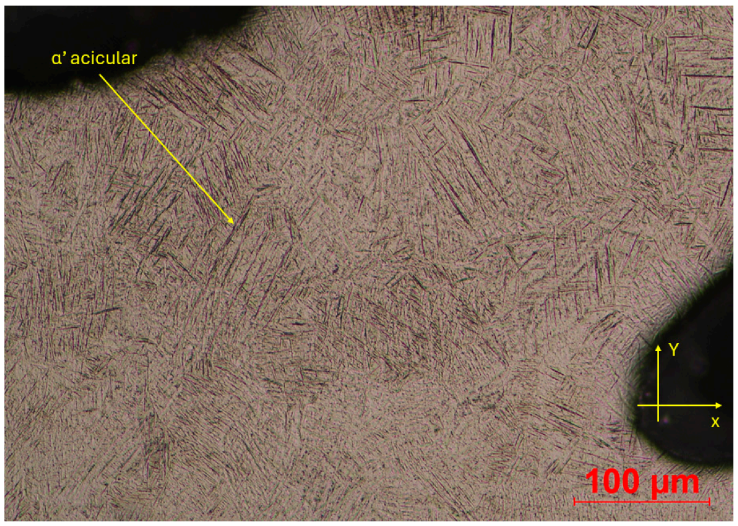


Figure 18. Micrograph of etched octet lattice joint.

SEM examination of the as-built lattice specimens revealed a highly irregular strut surface, with extensive adhesion of spherical and partially fused powder particles (Figure 19). At higher magnification, pronounced balling and local particle agglomeration were observed on the strut surfaces, together with local variations in the apparent strut diameter. These features contribute to the rough as-built surface morphology and may locally affect the dimensional accuracy of the lattice members.

Representative SEM observations of the metallographically prepared cross-sections further revealed irregular strut geometries, local variations in strut thickness, discontinuities, and internal porosity (Figure 20). Some struts exhibited substantial deviations from a uniform cross-sectional profile, which confirmed the presence of local geometrical non-uniformities within the as-built lattice. These observations, together with the surface features identified in the as-built specimens, indicate that further optimization of the

LPBF process parameters is required to improve the dimensional accuracy and structural continuity of the lattice struts.

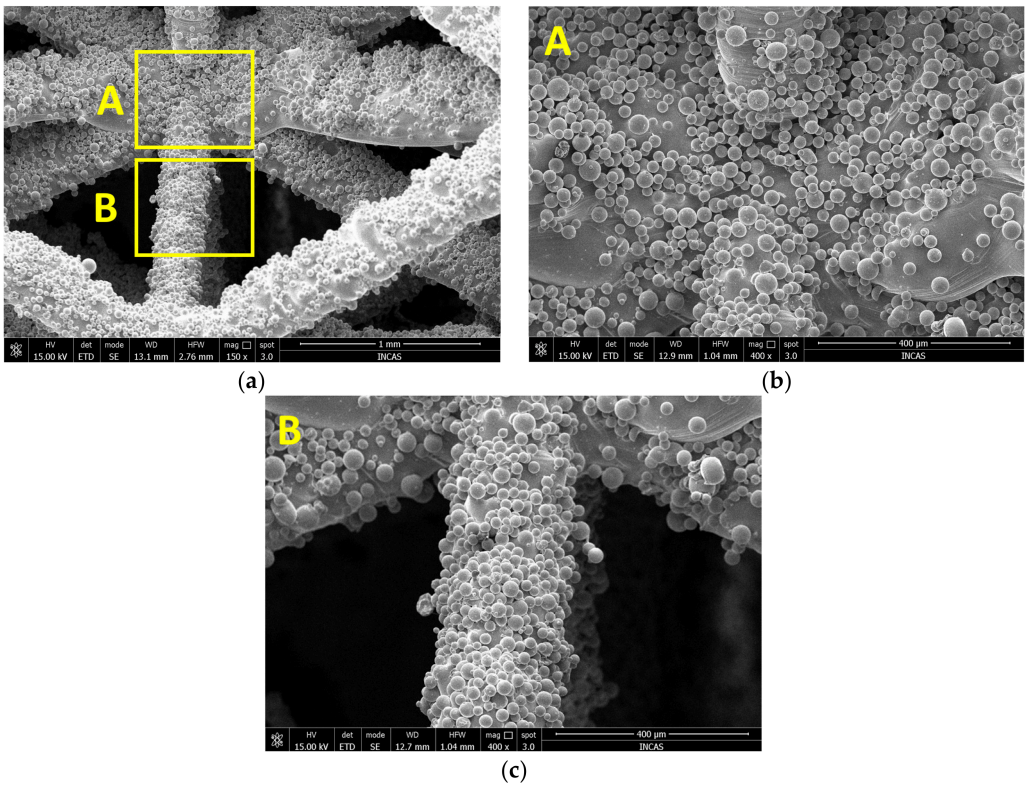


Figure 19. Representative SEM micrographs of the as-built Ti-6Al-4V lattice structure: (**a**) overall view of the strut network; (**b**) higher-magnification detail of Region A; and (**c**) higher-magnification detail of Region B, showing pronounced balling.

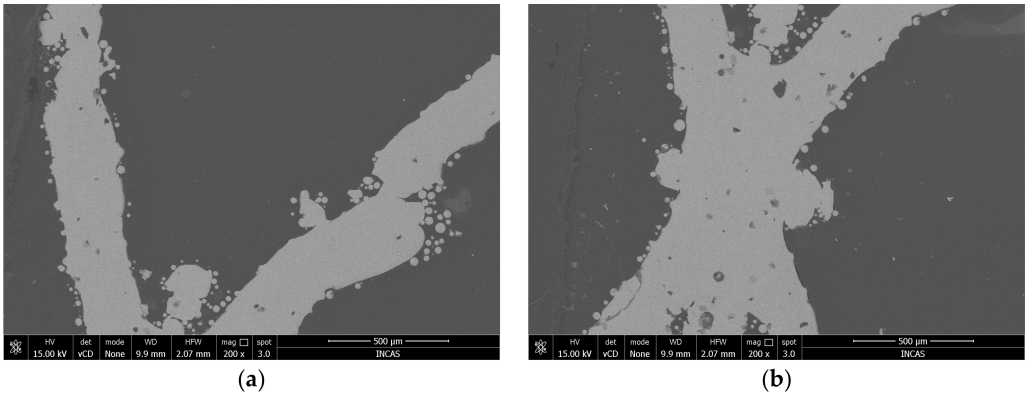


Figure 20. Representative SEM micrographs of metallographically prepared cross-sections of the Ti-6Al-4V lattice specimens, showing (**a**) irregular strut geometries, local thickness variations, discontinuities, and (**b**) internal porosity.

SEM examination of the compression-tested lattice specimens revealed a localized fracturing of individual struts associated with the progressive collapse of the lattice structure (Figure 21). Regions A and B show fractured members at different locations within the deformed lattice, with irregular fracture surfaces. Failure occurred through successive strut fracture and local instability rather than through uniform deformation of the entire lattice. This observation is consistent with the repeated load drops recorded during compression testing, associated with the progressive collapse of successive lattice regions.

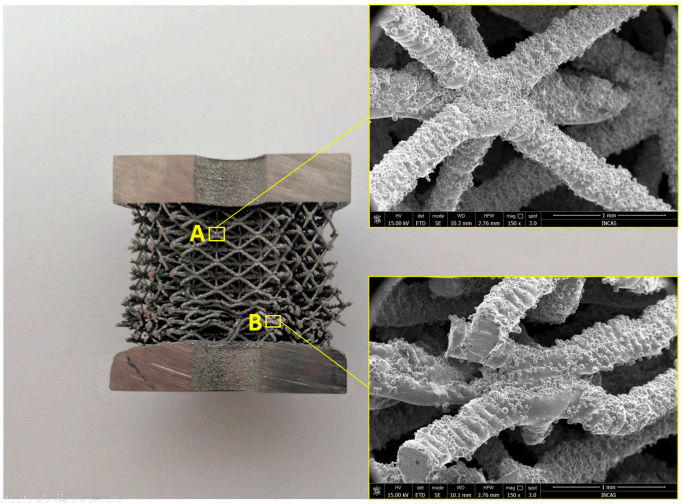


Figure 21. Representative post-compression appearance of the Ti-6Al-4V lattice specimen and SEM micrographs of selected regions A and B, showing localized strut fracture and progressive lattice collapse.

The CT scan investigation revealed pores distributed in the volume of both lattice configurations. In Figure 22a, the volume defect count is comprised mainly of defects under 2×10^{-3} cubic millimeters, with larger volume defects located in the supports area. Figure 22b shows a uniform distribution of the pores within the sample volume and mainly in strut locations. For the open-cell sample, the same distribution of the pores in the struts is observed, but with fewer counts (1300 vs. 7000) and with pores less than 0.03 mm^3. However, these absolute counts should be interpreted accordingly, as the specimens differ in material volume and architecture and the counts alone do not establish differences in relative defect content.

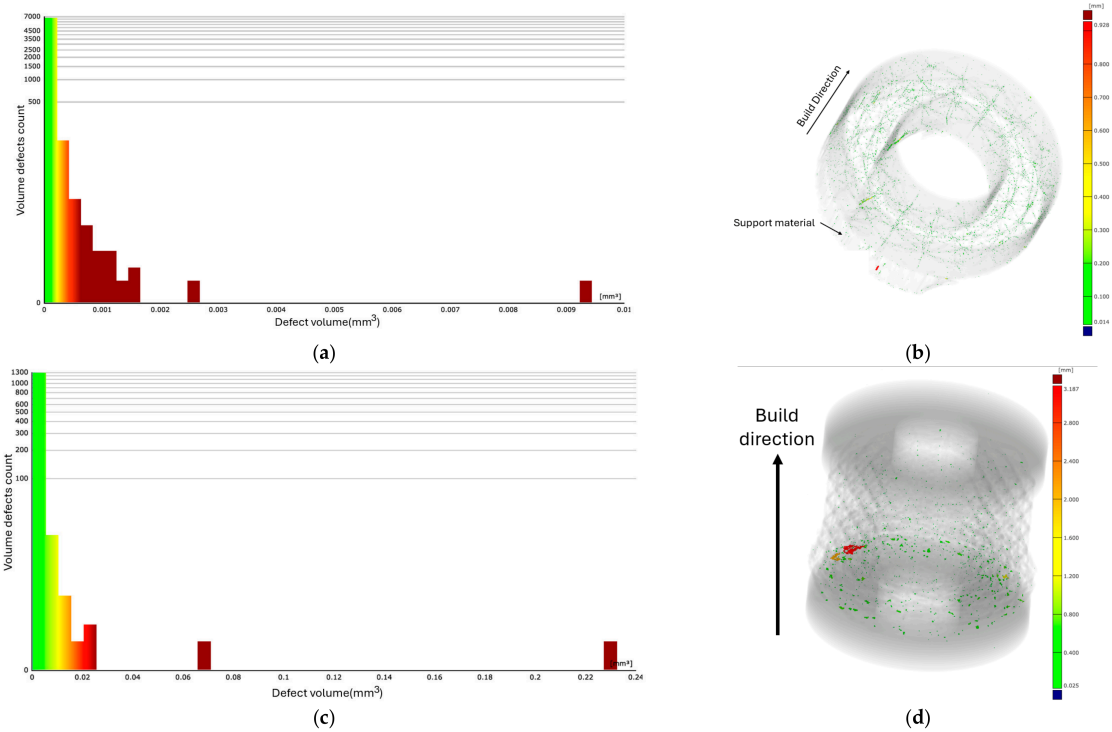


Figure 22. CT scan results of (**a**) shelled sample 0.25_S artifact with volume defects count; (**b**) distribution of defects within the analyzed sample 0.25_S; (**c**) open-cell sample 0.25_O volume defects count and (**d**) distribution of defects within the analyzed sample 0.25_O.

4. Discussion

The aim of this study was to determine the influence of strut diameter on the compressive strength of cylindrical mapped octet samples manufactured by LPBF from Ti-6Al-4V, which is extensively used in the aerospace industry. This study investigated a new way to increase the performance of lattice metamaterials to reach the structural performance of the bulk alloy. This study is responding to the great interest of the scientific community in studies concerning the optimization of lattice structures. The present study is of high importance especially for aerospace components subjected to rotation, like pumps, impellers, and shafts that require a cylindrical mapped lattice for dynamic balancing.

The scientific community is studying various concepts to increase the mechanical performance of lattice structures like hollow tube lattices [26,27], biomimicry [4,12,14,36] and the hybridization of lattice structures [2,6,11,17,37,38]. This work followed the hybridization approach but differs from the other works by introducing a reinforcement of relatively low complexity for AM. In [27], Lan et al. showed the effect of thickness on the yield strength under uniaxial compression of hollow octet lattices of 300 to 600 µm in thickness produced from SS316L and found the same trend as in Figures 7 and 9 observed for the open-cell cylindrical-coordinate generated lattices from this study. Zhang et al. found in [26] the same trend of increasing modulus and yield strength with the relative density of the lattice under uniaxial compression testing, similar to the findings in Figures 8 and 10. The stress–strain curves obtained on Cartesian generated lattices from [26] are similar to the ones determined in this work and presented in Figure 6, with the difference that after the reach of the maximum compressive stress, the curves in this work exhibit a periodic behavior generated by the failure of one lattice stage at a time determined by the strong stretch-dominant octet cell, while the curves from [26] present a mixed mode of both stretching and bending generated by the buckling of thin-walled tubes of the octet lattice. Studies from [26,27] and [7] investigated the mechanical response of Cartesian coordinate lattices in the 10–20% relative-density range, while this study went even deeper on the ultra-low-density side, ranging from 6 to 10% relative density. The reduction in relative density provides significant mass-reduction potential; however, it also increases the sensitivity of the mechanical response to the lattice architecture, strut dimensions, nodal geometry, and manufacturing-induced deviations. At these low densities, small variations in strut thickness can represent a comparatively large fraction of the load-bearing cross-section, potentially resulting in pronounced changes in stiffness, strength, and failure behavior. While the hollow tube strategy is effective in producing lightweight lattices with geometries suited for LPBF manufacturing, they suffer from a practical disadvantage of powder evacuation.

In Figure 23, a comparison of the open-cell and shelled samples shows a drastic increase in the compressive modulus of the shelled samples by a factor of almost 16 for the 0.25_S configuration over the open-cell one. The maximum compressive modulus was recorded for the 0.25_S sample with 6426 MPa.

By comparing the specific compressive modulus of the two configurations in Figure 24, it can be concluded that the shelled specimens (blue) are more rigid due to the effect of reinforcement, and even if the relative density of the shelled specimens is higher, the shelled specimens represent a much more structurally efficient solution than the open lattice (orange) alone. Both sample configurations follow the same trend of increasing up to a maximum and then decreasing in specific compressive modulus. For the open-cell samples, the maximum specific compressive modulus is reached for the 0.23_O sample, while for the shelled samples, the 0.25_S sample is the best-performing. The shell-only configuration (gray) provides an additional reference for assessing the contribution of the external shell independently of the lattice core. Its compressive modulus is approximately

3.44 MPa·m^3/kg, compared with 3.51 MPa·m^3/kg for the 0.21_S specimen. Thus, removing the lattice results in a reduction of 2.1% in the compressive modulus, while the measured density decreases by approximately 6%. This indicates that the shell-only configuration retains a specific stiffness close to that of the 0.21_S specimen, despite its lower density.

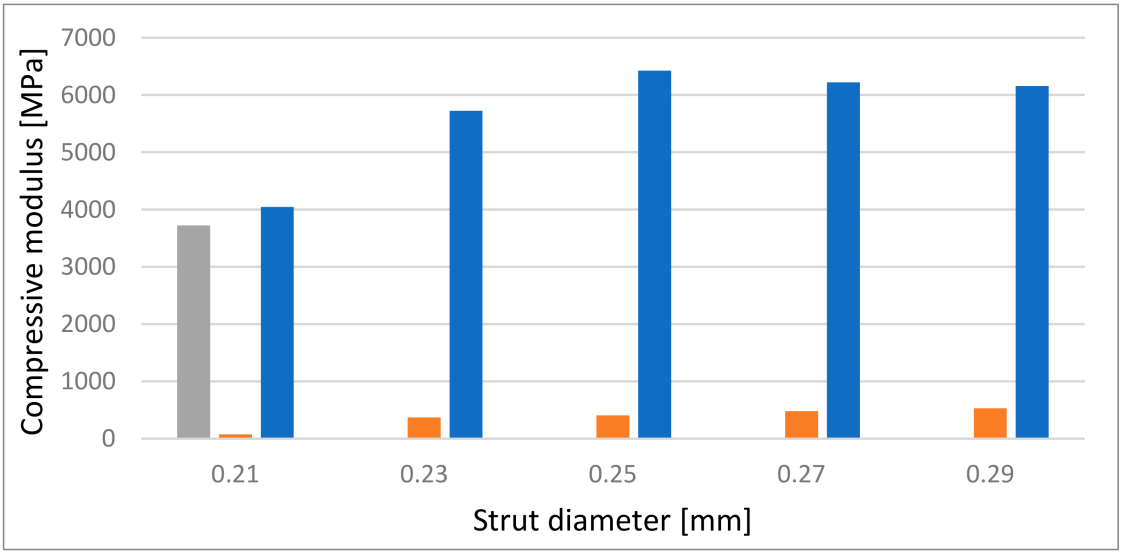


Figure 23. Comparison of compressive modulus of open-cell (orange), shelled (blue) and shell-only (gray) samples.

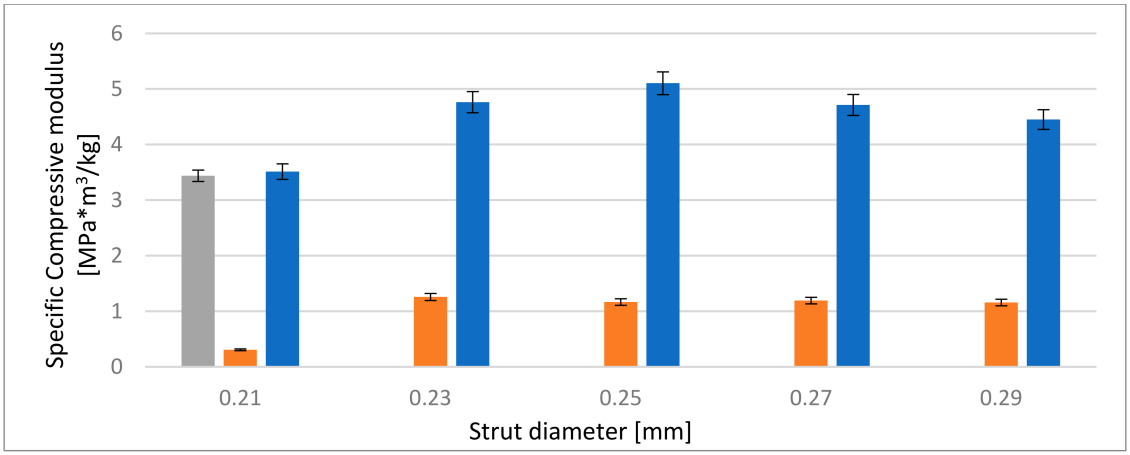


Figure 24. Comparative view of the specific compressive modulus of open-cell (orange), shelled (blue) and shell-only (gray) samples.

In Figure 25, a comparative analysis of the open-cell samples and the shelled ones is presented. It can be observed that the open-cell samples have a linear dependency of the strut diameter and specific compressive strength, while the shelled samples reach a maximum for the 0.25_S configuration, growing linearly from 0.21_S, and after that, a decrease in specific strength is observed. This indicates that for the shelled samples, the maximum structural performance is obtained for the 0.25 mm octet lattice, and increasing the strut diameter above this point is not beneficial. Compared to the open-cell samples, the shelled ones present a major increase in the specific strength, almost as efficient as solid titanium.

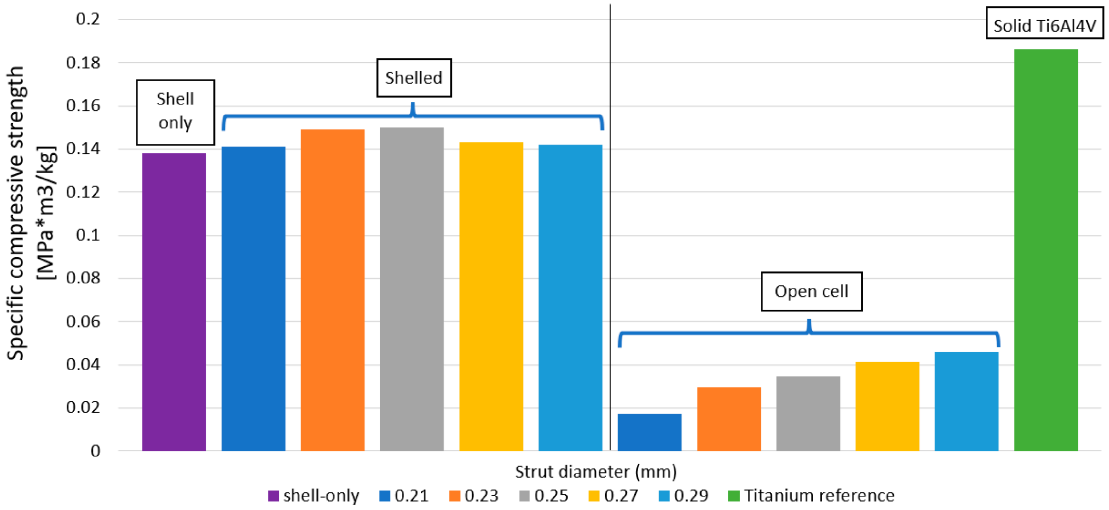


Figure 25. Comparison of specific strength of shelled and open-cell samples.

Despite the mechanical benefits provided by shell hybridization, the SEM observations highlight an important manufacturing consideration. The use of a single LPBF parameter set for both thin lattice struts and continuous shell regions may not provide optimal processing conditions for these geometrically different features. The observed surface irregularities, dimensional deviations, local discontinuities, and porosity suggest that feature-specific optimization of the LPBF parameters should be considered. Separate parameter sets for the lattice and shell regions could improve geometrical accuracy, surface quality, and structural integrity while preserving the mechanical advantages of the hybrid design.

5. Conclusions

This study investigated the effect of strut diameter in ultra-low-density Ti-6Al-4V octet lattice metamaterials generated using cylindrical mapping and the hybridization above the cell level using cylindrical shells of 500 μm thickness on the mechanical properties under compression loading of LPBF-manufactured samples. Based on the experimental, dimensional and numerical results, the following conclusions can be drawn:

- The strut diameter has a directly proportional relationship with the compressive strength and modulus of both types of samples.
- The cylindrical shell has a substantial contribution to the compressive strength and modulus.
- Shelled architectures exhibited over ten-fold increases in specific compressive strength and modulus compared with open-cell lattices. The shell-only results indicate that the outer shell dominates compressive performance, while the internal lattice provides a more modest additional improvement. These findings highlight the potential of shell–lattice hybridization for improving load-bearing efficiency at ultra-low relative densities, without implying equivalence to bulk Ti-6Al-4V.
- Gibson–Ashby relationships reasonably described the dependence of compressive properties on relative density but remain empirical for the investigated configurations. At ultra-low densities, deviations between nominal and manufactured strut dimensions introduce uncertainty in cell topology and mechanical performance.
- The best compressive performance was achieved by the shelled sample 0.29_S at 196 MPa and by open-cell sample 0.29_O at 21 MPa within the investigated configurations.
- The optical microscope measurements showed adhered particles to the lattice members that make the dimensional characterization of the ultra-low-density lattice struts difficult. This limitation highlights the importance of appropriate dimensional characteri-

zation for ultra-low-density LPBF lattices, where adhered particles and manufacturing deviations can represent a substantial fraction of the nominal strut dimensions.

The results suggest that a single LPBF parameter set is not necessarily optimal for both the lattice and hybrid shell–lattice regions. Future process development should therefore consider feature-specific parameter optimization for the lattice struts and shell regions in order to improve dimensional accuracy, surface quality, and structural integrity. Further studies can focus on other ultra-low-density cell types (TPMS, strut-based, hybrid cells, bioinspired cells, etc.) to determine the mechanical properties under various loading conditions, with special emphasis on dynamic loading (fatigue, impact, vibration, etc.) and the fabrication limits of the LPBF process of such samples in connection with common defects and mitigation strategies. Future research can focus on studying the influence and efficiency of the shelling strategy with other cell types on samples or components. Other alloy systems can be studied, including aluminum, nickel, high-entropy alloys (HEAs), etc. Another research direction should focus on the heat treatments of titanium alloy lattices to improve ductility. Finally, the local optimization of lattice junctions represents a promising direction for further investigation, particularly through optimized fillet or transition geometries at strut–strut and strut–shell junctions. Such approaches could be investigated specifically for ultra-low-density lattice structures, where local junction geometry may strongly influence stress concentration, load transfer, and failure initiation.

Supplementary Materials: The following supporting information can be downloaded at: https://www.mdpi.com/article/10.3390/app162110451/s1, Video S1: Sample_0.25_O_CT_scan; Video S2: Sample_0.25_S_CT_scan.

Author Contributions: Conceptualization, C.R.S. and A.P.; methodology, C.R.S. and A.P.; software, C.R.S. and V.-I.P.; validation, A.P. and S.G.B.; formal analysis, C.R.S.; investigation, C.R.S. and S.G.B.; resources, A.P.; data curation, A.P.; writing—original draft preparation, C.R.S.; writing—review and editing, C.R.S., A.P. and S.G.B.; visualization, C.R.S.; supervision, A.P.; project administration, A.P.; funding acquisition, A.P. All authors have read and agreed to the published version of the manuscript.

Funding: This work was supported by a grant from the Ministry of Research, Innovation and Digitalization, CCCDI-UEFISCDI, project number PN-IV-P7-7.1-PED-2024-2078 (Ctr. No. 34PED/2025), within PNCDI IV.

Institutional Review Board Statement: Not applicable.

Informed Consent Statement: Not applicable.

Data Availability Statement: The original contributions presented in this study are included in the article/Supplementary Materials. Further inquiries can be directed to the corresponding author.

Acknowledgments: The authors would like to thank Eng. Alina Dragomirescu from the National Institute for Aerospace Research "Elie Carafoli" (INCAS) for her support in performing the scanning electron microscopy (SEM) analysis.

Conflicts of Interest: The authors declare no conflicts of interest.

Abbreviations

The following abbreviations are used in this manuscript:

AM	additive manufacturing
AMed	additively manufactured
LPBF	laser powder bed fusion
RVE	representative volume element
TPMS	triply periodic minimal surfaces
HEA	high-entropy alloys

CT	computed tomography

References

1. Yang, W.; Yang, H.; Li, T. Additively manufactured mechanical meta-materials: Design and applications to aeroengine structures. *Int. J. Struct. Integr.* **2025**, *17*, 358–401. [CrossRef]
2. He, P.; Wen, Y.; Liang, X.; Du, X.; Feng, Y.; Di, Y.; Zhang, Y. Bio-inspired hybrid design and mechanical properties of 3D compression-twist coupling chiral lattice with functional integration. *Compos. Struct.* **2025**, *373*, 119670. [CrossRef]
3. Li, Y.; Yanming, F.; Li, D. Study on the dynamic response of octet-truss lattice composite sandwich panels on elastic foundations under blast and boundary loading. *Eur. J. Mech.-A/Solids* **2026**, *115*, 105836. [CrossRef]
4. Yarahmadi, A.; Nikaein, G.; Sadeghi, M.H. A bioinspired lattice bone scaffold with tunable transverse isotropy based on a modified octet–truss unit cell. *Forces Mech.* **2026**, *24*, 100373. [CrossRef]
5. Xie, Z.; Fu, X.; Zhang, Q.; Liu, L.; Zhu, X.; Ren, Y.; Chen, W. Ballistic performance of additive manufacturing metal lattice structures. *Thin-Walled Struct.* **2025**, *208*, 112763. [CrossRef]
6. Cui, Z.; Sun, Z.; Zhao, J.; Ding, Y.; Shim, V.P.W. Response of hybrid plate-rod lattices to static and dynamic compression–An experimental study. *Int. J. Impact Eng.* **2025**, *202*, 105321. [CrossRef]
7. Omar, R.; Noronha, J.; Haberl, E.; Dash, J.; Lu, S.; Wang, T.; Jiang, H.; Brandt, M.; Qian, M. Additive manufacturing of Ti-6242 lattice structures: Manufacturability limits and mechanical performance of solid and hollow strut architectures. *Mater. Sci. Eng. A* **2026**, *973*, 150662. [CrossRef]
8. Wu, M.; Linne, M.; Forien, J.-B.; Barton, N.R.; Ye, J.; Hazeli, K.; Perron, A.; Bertsch, K.; Wang, Y.M.; Voisin, T. Additively manufactured β-Ti5553 with laser powder bed fusion: Microstructures and mechanical properties of bulk and lattice parts. *J. Mater. Process. Technol.* **2024**, *327*, 118354. [CrossRef]
9. Bielski, P.; Doroszko, M.; Seweryn, A. Failure mechanisms and strength of mesostructurally modified Ti-6Al-4V lattice metamaterials designed for additive manufacturing. *Eng. Fail. Anal.* **2026**, *186*, 110478. [CrossRef]
10. Casata, M.; Garrido, C.; Wilkinson, T.; Perosanz, S.; Barba, D. Nodal geometry optimization in additively manufactured thin lattice structures: Application to the design of lightweight Ti–6Al–4V LPBF metamaterials. *Thin-Walled Struct.* **2026**, *221*, 114414. [CrossRef]
11. Wu, H.; Kwon, D.-S.; Yong, W.; Joo, H.; Jung, K.-H.; Lee, H.W.; Chen, W.; Kim, D.-K. Additively manufactured SS316L hybrid-architected metamaterials with enhanced strength and energy absorption. *Thin-Walled Struct.* **2026**, *218*, 114150. [CrossRef]
12. Yu, P.; Zhang, P.; Ma, H.; Chen, X.; Tan, H.; Kadic, M. Bio-inspired alternating collinear tubular lattice metamaterial for enhanced energy absorption and compressive stability. *Eng. Struct.* **2026**, *359*, 122715. [CrossRef]
13. Kishore, M.L.P. Computational and experimental investigation of lattice structures for tensile and compressive strength. *Next Mater.* **2026**, *11*, 101853. [CrossRef]
14. Li, D.; Sun, T.; Chen, B.; Zhang, X. Design and analysis of multiple bio-inspired aperiodic lattice structures by laser powder bed fusion. *Mater. Des.* **2025**, *253*, 113994. [CrossRef]
15. Mwema, F.; Ndou, N. Effect of the Strut Thickness on the Mechanical Properties, Deformation, and Failure Mechanisms of Vascular Bundle–Inspired Structures. *Eng. Rep.* **2026**, *8*, e70622. [CrossRef]
16. Azim, E.; Islam, M.R. Distinct regimes of mechanical reinforcement in lattice network-based interpenetrating phase composites. *Mech. Mater.* **2026**, *216*, 105640. [CrossRef]
17. Emir, E.; Bahçe, E. Compressive behavior of functional graded hybrid lattice structure. *Int. J. Adv. Manuf. Technol.* **2025**, *138*, 1605–1620. [CrossRef]
18. Xiong, J.; Ma, L.; Vaziri, A.; Yang, J.; Wu, L. Mechanical behavior of carbon fiber composite lattice core sandwich panels fabricated by laser cutting. *Acta Mater.* **2012**, *60*, 5322–5334. [CrossRef]
19. Li, Y.; Dias Filho, J.M.; Dehgahi, S.; Butt, S.U.; Henein, H.; Qureshi, A.J. Hybrid investment casting of Al-Cu-Sc alloy-based lattice structures: Material and process characterization. *Adv. Ind. Manuf. Eng.* **2025**, *10*, 100160. [CrossRef]
20. Yang, J.; Huang, Z.; Yuan, L.; Li, W. Laser powder bed fusion of bio-inspired rotational lattice metamaterial with advanced mechanical performance. *J. Mater. Res. Technol.* **2025**, *35*, 4510–4519. [CrossRef]
21. Gupta, S.; Kandasubramanian, B.; Gnanamoorthy, R.; Kchaou, M. Structure–property correlations in digitally manufactured polymeric octet lattices. *Polymer* **2026**, *355*, 129951. [CrossRef]
22. Sokollu, O.B.; Gulcan, O.; Konukseven, E.I. Mechanical Properties Comparison of Strut-Based and Triply Periodic Minimal Surface Lattice Structures Produced by Electron Beam Melting. *Addit. Manuf.* **2022**, *60*, 103199. [CrossRef]
23. Gibson, L.J.; Ashby, M.F. *Cellular Solids: Structure and Properties*, 2nd ed.; Cambridge University Press: Cambridge, UK, 1997. [CrossRef]
24. Deshpande, V.S.; Ashby, M.F.; Fleck, N.A. Foam topology: Bending versus stretching dominated architectures. *Acta Mater.* **2001**, *49*, 1035–1040. [CrossRef]

25. Condruz, M.R.; Badea, T.A.; Paraschiv, A. Compressive Behavior of Inconel 625 and Ti-6Al-4V Strut Lattices Fabricated by LPBF. *Appl. Sci.* **2024**, *14*, 11909. [CrossRef]
26. Zhang, P.; Chen, X.; Yu, P.; Zhao, K.; Ma, H.; Liu, S.; Tan, H.; Laude, V.; Kadic, M. Grid hollow octet truss lattices that are stable at low relative density. *J. Mech. Phys. Solids* **2025**, *197*, 106068. [CrossRef]
27. Lan, T.; Al-Ketan, O.; Tran, P. Controlled deformation of metallic hollow octet-truss lattice structures. *Thin-Walled Struct.* **2026**, *223*, 114639. [CrossRef]
28. Thirupathi, S.; Dixit, A.R.; Shaw, P.K.; Dwivedi, S. Optimization of Ti-6Al-4V alloy lattice structures using simulation-based machine learning for enhanced mechanical properties in laser powder bed fusion. *Mater. Lett.* **2025**, *385*, 138166. [CrossRef]
29. Iandiorio, C.; Mattei, G.; Marotta, E.; Costanza, G.; Tata, M.E.; Salvini, P. The beneficial effect of a TPMS-based fillet shape on the mechanical strength of metal cubic lattice structures. *Materials* **2024**, *17*, 1553. [CrossRef] [PubMed]
30. Zhu, Y.; Xu, F.; Zou, Z.; Dai, X. Tunable compression response and enhanced mechanical properties of bio-inspired lattice structures with dual-stage stiffness. *Eur. J. Mech.-A/Solids* **2026**, *116*, 105911. [CrossRef]
31. Ferro, C.G.; Varetti, S.; Maggiore, P. Experimental Evaluation of Mechanical Compression Properties of Aluminum Alloy Lattice Trusses for Anti-Ice System Applications. *Machines* **2024**, *12*, 404. [CrossRef]
32. *F3302*; Standard for Additive Manufacturing—Finished Part Properties—Standard Specification for Titanium Alloys via Powder Bed Fusion. ASTM International: West Conshohocken, PA, USA, 2018. Available online: https://store.astm.org/f3302-18.html (accessed on 18 August 2026).
33. *ISO 13314:2011*; Mechanical Testing of Metals—Ductility Testing—Compression Test for Porous and Cellular Metals. International Organization for Standardization: Geneva, Switzerland, 2011.
34. *ASTM E9-19*; Standard Test Methods of Compression Testing of Metallic Materials at Room Temperature. ASTM International: West Conshohocken, PA, USA, 2019.
35. Bellini, C.; Borrelli, R.; Di Caprio, F.; Di Cocco, V.; Franchitti, S.; Iacoviello, F.; Sorrentino, L. An Innovative Method to Analyse the Geometrical Accuracy of Ti6Al4V Octet-Truss Lattice Structures. *Materials* **2023**, *16*, 2372. [CrossRef] [PubMed]
36. Zhao, L.; Zhang, R.; Kong, Q.; Yu, M.; Wen, L. Synergistic collapse design of a multi-feature bioinspired lattice for multifunctional mechanical optimization. *Mater. Des.* **2026**, *261*, 115344. [CrossRef]
37. Rahimi, S.; Asghari, M. Design and evaluation of two proposed hybrid FCC-BCC lattice structures for enhanced mechanical performance. *Heliyon* **2025**, *11*, e40911. [CrossRef] [PubMed]
38. Wu, Q.; Zhang, X.; Wu, B.; Sun, Z.; Li, K.; Ding, Y. Energy absorption and deformation mechanism of hybrid tube-rod lattice sandwich structures under local loadings. *Compos. Struct.* **2026**, *389*, 120407. [CrossRef]

Disclaimer/Publisher's Note: The statements, opinions and data contained in all publications are solely those of the individual author(s) and contributor(s) and not of MDPI and/or the editor(s). MDPI and/or the editor(s) disclaim responsibility for any injury to people or property resulting from any ideas, methods, instructions or products referred to in the content.